Available online at www.sciencedirect.com
ScienceDirect
Journal of Computational Physics 227 (2008) 2430–2454
JOURNAL OF COMPUTATIONAL PHYSICS
www.elsevier.com/locate/jcp

A Hermite upwind WENO scheme for solving hyperbolic conservation laws

G. Capdeville *

Laboratoire de Mécanique des fluides, Ecole Centrale de Nantes, 1, rue de la Noë, B.P. 92101, 44321 Nantes cedex 3, France

Received 13 December 2006; received in revised form 18 October 2007; accepted 22 October 2007
Available online 1 November 2007

Abstract

This paper proposes a new WENO procedure to compute problems containing both discontinuities and a large disparity of characteristic scales.

In a one-dimensional context, the WENO procedure is defined on a three-points stencil and designed to be sixth-order in regions of smoothness. We define a finite-volume discretization in which we consider the cell averages of the variable and its first derivative as discrete unknowns. The reconstruction of their point-values is then ensured by a unique sixth-order Hermite polynomial. This polynomial is considered as a symmetric and convex combination, by ideal weights, of three fourth-order polynomials: a central polynomial, defined on the three-points stencil, is combined with two polynomials based on the left and the right two-points stencils.

The symmetric nature of such an interpolation has an important consequence: the choice of ideal weights has no influence on the properties of the discretization. This advantage enables to formulate the Hermite interpolation for non-uniform meshes. Following the methodology of the classic WENO procedure, nonlinear weights are then defined.

To deal with the peculiarities of the Hermite interpolation near discontinuities, we define a new procedure in order for the nonlinear weights to smoothly evolve between the ideal weights, in regions of smoothness, and one-sided weights, otherwise.

The resulting scheme is a sixth-order WENO method based on central Hermite interpolation and TVD Runge–Kutta time-integration. We call this scheme the HCWENO6 scheme.

Numerical experiments in the scalar and the 1D Euler cases make it possible to check and to validate the options selected. In these experiments, we emphasize the resolution power of the method by computing test cases that model realistic aero-acoustic problems.

Keywords: Hermite polynomial; Central WENO interpolation; Hyperbolic systems; Non-uniform meshes; Upwind discretization

* Tel.: +33 2 4037 1651; fax: +33 2 4037 2523.
E-mail address: guy.capdeville@ec-nantes.fr

0021-9991/$ - see front matter
doi:10.1016/j.jcp.2007.10.017

1. Introduction

Nowadays, high-order computational methods are highly demanded for solving problems in computational fluid dynamics (CFD). For flow problems with intricate structures and a very broad range of characteristic scales, high resolution is necessary in order for the structural information to be correctly extracted.

For example, in the direct numerical simulation (DNS) and the large eddy simulation (LES) of turbulence, it is required that the numerical schemes be highly accurate. Computational aero-acoustics (CAA) is another area where high-resolution schemes are required. Moreover, if the flow fields involve shock waves, those schemes should also be non-oscillatory near the discontinuities without leading to an excessive damping of the turbulent or acoustic fluctuations, [19].

Weighted essentially non-oscillatory (WENO) schemes are one class of high-order numerical schemes. Historically, WENO schemes are based upon the successful essentially non-oscillatory (ENO) schemes that started with the henceforth-classic paper of Harten et al. in 1987, [1].

However, WENO schemes improve upon ENO schemes in robustness, smoothness of the numerical fluxes, convergence properties and computational efficiency. Owing to these advantages, a large variety of WENO schemes was designed in recent years; see [2] for a good overview.

Nevertheless, in spite of a vast field of application, numerical tests indicate that classical WENO schemes are usually not optimal for computing turbulent flows or aero-acoustic fields because they can lead to a significant damping of the turbulent or acoustic fluctuations.

A way to improve the dissipation properties of a WENO scheme consists in reducing its stencil width. Indeed, the compactness of a numerical stencil owes many advantages: firstly, boundary conditions and complex geometries are easier to deal with; secondly, for the same formal accuracy, compact stencils are known to exhibit significantly more resolution of the smaller scales by improving the dispersive and the dissipative properties of the numerical scheme, [4,3].

Mainly, there are two ways for increasing the compactness of a numerical stencil. Based on Lele's work, [3], a first approach consists in using compact high-order schemes which consider as unknowns, at each discretization point, not only the value of the function but also those of its first or higher derivatives. Compact schemes are very accurate in smooth regions with spectral-like resolution, but are known to produce non-physical oscillations when they are applied directly to flow with discontinuities. A solution is to use compact schemes coupled with the non-oscillatory properties of WENO schemes, [5,6].

Selecting this solution, the non-oscillatory shock-capturing schemes are only used locally near the discontinuities and the compact schemes are employed in regions of smoothness. Thus, a hybrid compact-WENO scheme combines the advantages of the compact schemes in smooth regions with a sharp representation of discontinuities.

However, compact schemes are implicit schemes: an algebraic linear system must be solved to obtain the spatial derivatives at any point. Lastly, those schemes are difficult to extend to non-uniform meshes.

Another way for increasing the compactness of a numerical stencil consists in evolving in time not only the primitive variable but also its derivatives. Then, more than one degree of freedom per cell is considered. For this purpose, a Hermite polynomial is usually defined to interpolate the solution and its derivatives.

In 1977, Van-Leer was the first one to study in details such schemes in a finite-difference context, [4]. He clearly demonstrated the advantages in using more numerical information inside the mesh: for the same given order of consistency, dispersive and dissipative errors are lowered if one uses such schemes. Since Van-Leer's paper, much work was done in this direction; for example see [7–9], in the recent years.

More recently, Qiu and Shu proposed a fifth-order WENO scheme based on Hermite polynomials for solving 1D nonlinear conservation laws systems, [10,11]. In a finite-volume context and following the original WENO philosophy, [2], the function and its first derivative are evolved in time and used in the polynomial reconstruction. Two Hermite polynomials are then defined: the first one is used to calculate the point-values of the solution from cell averages; the second Hermite polynomial enables the calculation of the point-values of the first derivative. In order for both reconstructions to be non-oscillatory, Qiu and Shu calculate nonlinear weights, according to [2]. The ideal weights that characterize the fifth-order accuracy are calculated for uniform meshes and are different from one polynomial to another.

Doing so, a fifth-order upwind reconstruction (HUWENO5) method is generated with only three-points for the numerical stencil. In this paper, we follow this direction of research.

In a finite-volume framework, we construct a sixth-order non-oscillatory scheme for solving 1D nonlinear hyperbolic systems of conservation laws. This scheme lies upon a central and local Hermite WENO interpolation.

To generate such a scheme, we use and extend the ideas of Levy et al. [12]. In their paper, the authors introduced a new central weighted non-oscillatory (CWENO) reconstruction. This new reconstruction is based on defining a suitable quadratic function that is added to linear polynomials to obtain third-order accuracy in smooth regions. In regions with discontinuities or large gradients, the weights are automatically and smoothly changed so that they switch to a one-sided second-order linear reconstruction. This reconstruction turns out to be extremely compact; in the one-dimensional case, the reconstruction is based on a three-point stencil. The main advantage of this procedure is that the choice of ideal weights has no influence on the properties of the discretization. Any symmetric choice of the constants defining the ideal weights will provide the desired accuracy. This property must be contrasted with classical upwind WENO reconstructions.

To maintain this property and to increase the accuracy on the same stencil (three-points for the one-dimensional problem), we develop a specific non-oscillatory Hermite polynomial based on the variable and its first derivative.

For this purpose, three polynomials are defined: two third degree polynomials based on a left and a right two-point stencil and a fifth-degree central polynomial based on the three-points stencil. This latter polynomial is necessary for the accurate recovery of the point-values in regions of smoothness. A convex combination by ideal and symmetric weights of those polynomials enables to define the sixth-order optimum polynomial on the three-points stencil.

To complete the non-oscillatory reconstruction, the calculation of the nonlinear weights is defined. Owing to the peculiarities of the Hermite interpolation, we need to define a new procedure for the nonlinear weights to evolve smoothly between the ideal and the one-sided weights.

While comparing with the HUWENO5 of Qiu and Shu, [10], the scheme we proposed has several significant differences:

- A unique Hermite polynomial is used to interpolate both the variable and its derivative.
- The same nonlinear weights are defined for both the variable and its first derivative.
- The procedure can be extended to non-uniform meshes with large stretching, without generating negative weights and without resorting to metric transformations. The high-resolution properties of the method are then maintained on such meshes.
- The resulting finite-volume scheme is sixth-order in smooth regions, fourth-order close to the singularities and, when that becomes necessary, first-order at the place of a discontinuity.

This paper is organized as follows: we start in Section 2 by defining the finite-volume framework of the method. In Section 3, we detail the construction and implementation of the HCWENO6 scheme, for 1D scalar and 1D Euler equations. Hermite interpolations are defined on non-uniform meshes; the specific procedure to generate a non-oscillatory reconstruction is then emphasized.

In Section 4, we select numerical tests to validate the method. Asymptotic analysis stability is first managed, to check the influence of the boundary conditions, the stretching of the mesh and possible source terms. The scheme is then tested by computing solutions of scalar nonlinear and 1D Euler equations. Emphasis is put on the resolution power of the method by computing cases that model realistic aero-acoustic configurations.

2. Governing equations and finite-volume framework

2.1. Governing equations

Let the following scalar nonlinear hyperbolic problem defined over the domain, Ω:

$$\begin{cases} u_t + f(u)_x = 0 \quad \forall x \in \Omega \\ u(x, t=0) = u_0(x) \end{cases} \tag{1}$$

Let $r \equiv u_x$ and $g(u,r) \equiv f'(u) \times u_x = f'(u) \times r$.

Then by deriving (1), we can define the new nonlinear hyperbolic problem over Ω:

$$\begin{cases} u_t + f(u)_x = 0, & u(x, t=0) = u_0(x) \\ r_t + g(u,r)_x = 0, & r(x, t=0) = u_0'(x) \end{cases} \tag{2}$$

Since $g(u,r) = f'(u) \times r$, this implies that the characteristic velocity, $\frac{\partial g}{\partial r}$, of the equation for the derivative variables, r, is $f'(u)$. Consequently, both equations constituting (2) share the same characteristic velocity: this result is used in what follows to generate a simple approximate Riemann solver discretizing (2).

Defining the discrete cell $I_i \equiv [x_{i-1/2}, x_{i+1/2}]$, Ω is partitioned in N non-overlapping cells: $\Omega = \bigcup_{i=1}^{N} I_i$. The non-uniform cell size is calculated as $\Delta x_i \equiv x_{i+1/2} - x_{i-1/2}$.

Lastly, we define the discrete cell averages of u and r as $\bar{u}_i \equiv \frac{1}{\Delta x_i} \int_{I_i} u(x,t)\mathrm{d}x$, $\bar{r}_i \equiv \frac{1}{\Delta x_i} \int_{I_i} r(x,t)\mathrm{d}x$.

Integrating (2) over I_i produces the following system of ordinary differential equations (ODE) for the variables $\bar{u}_i, \bar{r}_i$:

$$\begin{cases} \frac{\mathrm{d}\bar{u}_i}{\mathrm{d}t} = -\frac{1}{\Delta x_i}[f(u(x_{i+1/2},t)) - f(u(x_{i-1/2},t))] \\ \frac{\mathrm{d}\bar{r}_i}{\mathrm{d}t} = -\frac{1}{\Delta x_i}[g(u(x_{i+1/2},t), r(x_{i+1/2},t)) - g(u(x_{i-1/2},t), r(x_{i-1/2},t))] \end{cases} \tag{3}$$

By using the classical "method of lines", time and space are separately discretized.

2.2. Spatial approximation: the numerical fluxes

Following the finite-volume methodology for generating a numerical scheme, the fluxes for u and r are approximated according to

$$\begin{cases} f(u(x_{i+1/2},t)) \approx \tilde{f}_{i+1/2} \equiv \tilde{f}\left(u^{\mathrm{L}}_{i+1/2}, u^{\mathrm{R}}_{i+1/2}\right) \\ g(u(x_{i+1/2},t), r(x_{i+1/2},t)) \approx \tilde{g}_{i+1/2} \equiv \tilde{g}\left(u^{\mathrm{L}}_{i+1/2}, r^{\mathrm{L}}_{i+1/2}, u^{\mathrm{R}}_{i+1/2}, r^{\mathrm{R}}_{i+1/2}\right) \end{cases} \tag{4}$$

$u^{\mathrm{L,R}}_{i+1/2}$ (resp. $r^{\mathrm{L,R}}_{i+1/2}$) represent the numerical approximations to the functions $u(x,t)$ (resp. $r(x,t)$) at the left and the right of the interface $x = x_{i+1/2}$, Fig. 1. The way of constructing the numerical fluxes, $\tilde{f}$, $\tilde{g}$, defines the upwind method.

To calculate those numerical fluxes, we selected the HLL (Harten, Lax and Van-Leer) approximate Riemann solver, [17].

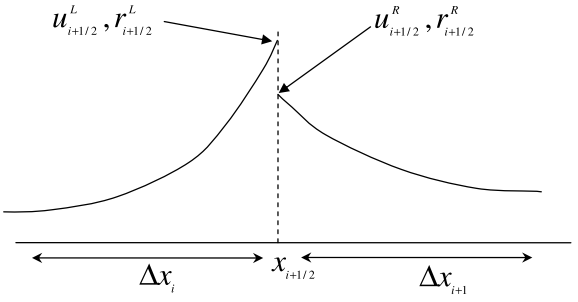

Fig. 1. Reconstruction of the point-values from cell averages at the interface $x = x_{i+1/2}$.

Thus, we get the following expressions for the numerical fluxes $\tilde{f}$ and $\tilde{g}$:

$$\begin{cases} \tilde{f}_{i+1/2} = \frac{\lambda^+_{i+1/2} f(u^{\mathrm{L}}_{i+1/2}) - \lambda^-_{i+1/2} f(u^{\mathrm{R}}_{i+1/2})}{\lambda^+_{i+1/2} - \lambda^-_{i+1/2}} + \frac{\lambda^+_{i+1/2} \times \lambda^-_{i+1/2}}{\lambda^+_{i+1/2} - \lambda^-_{i+1/2}} \left(u^{\mathrm{R}}_{i+1/2} - u^{\mathrm{L}}_{i+1/2} \right) \\ \tilde{g}_{i+1/2} = \frac{\lambda^+_{i+1/2} g(u^{\mathrm{L}}_{i+1/2}, v^{\mathrm{L}}_{i+1/2}) - \lambda^-_{i+1/2} g(u^{\mathrm{R}}_{i+1/2}, v^{\mathrm{R}}_{i+1/2})}{\lambda^+_{i+1/2} - \lambda^-_{i+1/2}} + \frac{\lambda^+_{i+1/2} \times \lambda^-_{i+1/2}}{\lambda^+_{i+1/2} - \lambda^-_{i+1/2}} \left(v^{\mathrm{R}}_{i+1/2} - v^{\mathrm{L}}_{i+1/2} \right) \end{cases} \tag{5}$$

With, in the scalar case, the following choices for the characteristic velocities $\lambda^{\pm}_{i+1/2}$:

$$\begin{cases} \lambda^+_{i+1/2} \equiv \max \left(f'(u^{\mathrm{L}}_{i+1/2}), f'(u^{\mathrm{R}}_{i+1/2}), 0 \right) \\ \lambda^-_{i+1/2} \equiv \min \left(f'(u^{\mathrm{L}}_{i+1/2}), f'(u^{\mathrm{R}}_{i+1/2}), 0 \right) \end{cases} \tag{6}$$

2.3. Time-integration scheme: the RGK3-TVD scheme

The discretization of the spatial operator generates an algebraic system of ODEs in time, for the discrete unknowns $(\bar{u}_i, \bar{r}_i)$.

If we define the followings spatial operators:

$$\begin{cases} F(\bar{u}, \bar{r})|_i \equiv -\frac{1}{\Delta x_i} [\tilde{f}_{i+1/2} - \tilde{f}_{i-1/2}] \\ G(\bar{u}, \bar{r})|_i \equiv -\frac{1}{\Delta x_i} [\tilde{g}_{i+1/2} - \tilde{g}_{i-1/2}] \end{cases} \tag{7}$$

Then we obtain the following system of ODEs:

$$\begin{cases} \frac{\mathrm{d}\bar{u}_i}{\mathrm{d}t} = F(\bar{u}, \bar{r})|_i \\ \frac{\mathrm{d}\bar{r}_i}{\mathrm{d}t} = G(\bar{u}, \bar{r})|_i \end{cases} \tag{8}$$

This system is integrated by a third-order TVD Runge–Kutta scheme, [13].

The general algorithm is

$$\begin{cases} \phi_i^{(1)} = \phi_i^n + \Delta t \times L(\phi^n) \\ \phi_i^{(2)} = \frac{3}{4}\phi_i^n + \frac{1}{4}\phi_i^{(1)} + \frac{\Delta t}{4} \times L(\phi^{(1)}) \\ \phi_i^{n+1} = \frac{1}{3}\phi_i^n + \frac{2}{3}\phi_i^{(2)} + \frac{2\Delta t}{3} \times L(\phi^{(2)}) \end{cases} \tag{9}$$

with the following associated definitions: $\phi \equiv \begin{cases} \bar{u} \\ \bar{r} \end{cases}$ and $L \equiv \begin{cases} F(\bar{u}, \bar{r}) \\ G(\bar{u}, \bar{r}) \end{cases}$.

3. Non-oscillatory reconstruction: the HCWENO6 scheme

3.1. Reconstruction from cell averages $(\bar{u}_i, \bar{r}_i)$

To begin, we select an optimal Hermite polynomial of degree 5, denoted by $\tilde{u}_{\mathrm{opt}}(x)$, on the central stencil $\{I_{i-1}, I_i, I_{i+1}\}$, Fig. 2: $\tilde{u}_{\mathrm{opt}}(x) \equiv \sum_{j=1}^{6} a_{j-1}(x - x_i)^{j-1}$.

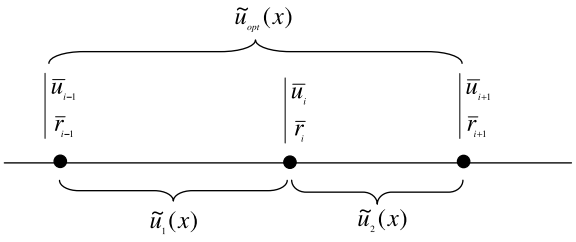

Fig. 2. Central, left and right stencils for the HCWENO6 procedure.

Following [1], $\tilde{u}_{\text{opt}}(x)$ is uniquely defined by the relations:

$$\begin{cases} \frac{1}{\Delta x_{i+k}} \int_{I_{i+k}} \tilde{u}_{\text{opt}}(x)\mathrm{d}x = \bar{u}_{i+k} \\ \frac{1}{\Delta x_{i+k}} \int_{I_{i+k}} \frac{\mathrm{d}}{\mathrm{d}x}\tilde{u}_{\text{opt}}(x)\mathrm{d}x = \bar{r}_{i+k} \end{cases} \quad k \in \{-1, 0, 1\} \tag{10}$$

Thus, we generated a linear system for the undetermined coefficients $\{a_j\}$.

This system can be re-written as

$$\mathbf{U} = \mathbf{C} \times \mathbf{A} \tag{11}$$

with the following notations:

$$\mathbf{U} \equiv [\bar{u}_{i-1}, \bar{u}_i, \bar{u}_{i+1}, \bar{r}_{i-1}, \bar{r}_i, \bar{r}_{i+1}]^t$$

$$\mathbf{A} \equiv [a_j]^t_{j\in\{0,\ldots,5\}}$$

$$\mathbf{C} \equiv \begin{bmatrix} c_{1j} = \frac{(-1)^j}{j\Delta x_{i-1}}\left[\left(\frac{\Delta x_i}{2}\right)^j - \left(\Delta x_{i-1} + \frac{\Delta x_i}{2}\right)^j\right] \\ c_{2j} = \frac{(\Delta x_i)^{j-1}}{j2^j}(1 + (-1)^{j+1}) \\ c_{3j} = \frac{1}{j\Delta x_{i+1}}\left[\left(\Delta x_{i+1} + \frac{\Delta x_i}{2}\right)^j - \left(\frac{\Delta x_i}{2}\right)^j\right] \\ c_{4j} = \frac{(-1)^{j-1}}{\Delta x_{i-1}}\left[\left(\frac{\Delta x_i}{2}\right)^{j-1} - \left(\Delta x_{i-1} + \frac{\Delta x_i}{2}\right)^{j-1}\right] \\ c_{5j} = \frac{(\Delta x_i)^{j-2}}{2^{j-1}}(1 + (-1)^j) \\ c_{6j} = \frac{1}{\Delta x_{i+1}}[(\Delta x_{i+1} + \frac{\Delta x_i}{2})^{j-1} - \left(\frac{\Delta x_i}{2}\right)^{j-1}] \end{bmatrix} \quad j \in \{1 \ldots 6\}$$

For solving the Riemann's problem (4), we only need the approximations to the values of $(u(x), r(x))$ at the cell boundaries.

Those values are calculated by

$$\begin{cases} u^{\mathrm{L}}_{i+1/2} = ({}^t\mathbf{D} \times C^{-1}) \times U \equiv \sum_{j=1}^{3} \tilde{a}_j \bar{u}_{i+j-2} + \sum_{j=4}^{6} \tilde{a}_j \bar{r}_{i+j-5} \\ r^{\mathrm{L}}_{i+1/2} = ({}^t\mathbf{E} \times C^{-1}) \times U \equiv \sum_{j=1}^{3} \tilde{b}_j \bar{u}_{i+j-2} + \sum_{j=4}^{6} \tilde{b}_j \bar{r}_{i+j-5} \end{cases} \tag{12}$$

with the following definitions: $\mathbf{D} \equiv \left[\left(\frac{\Delta x_i}{2}\right)^{j-1}\right]_{j=1\ldots6}$, $\mathbf{E} \equiv \left[(j-1)\left(\frac{\Delta x_i}{2}\right)^{j-2}\right]_{j=1\ldots6}$

The constants $\{\tilde{a}_j, \tilde{b}_j\}$ depend on the cell sizes, Δx_i, but not on the function u or r itself. Practically, those constants are pre-computed in the case of a non-uniform grid and stored before solving the PDEs.

For the calculations of $u^{\mathrm{R}}_{i-1/2}$ and $r^{\mathrm{R}}_{i-1/2}$, the constants $\{\tilde{a}_j, \tilde{b}_j\}$ are simply calculated by modifying the form of the vectors $\mathbf{D}$ and $\mathbf{E}$:

$$\mathbf{D} \equiv \left[(-1)^{j+1}\left(\frac{\Delta x_i}{2}\right)^{j-1}\right]_{j=1\ldots6}, \quad \mathbf{E} \equiv \left[(-1)^j(j-1)\left(\frac{\Delta x_i}{2}\right)^{j-2}\right]_{j=1\ldots6}$$

Finally, the calculated point-values at the cell boundary $x = x_{i+1/2}$ are such that

$$\begin{cases} u_{i+1/2} = u(x_{i+1/2}) + \mathrm{O}(\Delta x^6) \\ r_{i+1/2} = \frac{\mathrm{d}}{\mathrm{d}x}u(x_{i+1/2}) + \mathrm{O}(\Delta x^5) \end{cases} \tag{13}$$

To derive an essentially non-oscillatory reconstruction, we need to define two supplementary polynomials approximating $(u(x), r(x))$ with a lower accuracy on I_i.

Thus, we define the third-degree polynomial, $\tilde{u}_1(x)$, on the reduced stencil $\{I_{i-1}, I_i\}$ whereas the third-degree polynomial, $\tilde{u}_2(x)$, is defined on the stencil $\{I_i, I_{i+1}\}$ (see Fig. 2).

3.2. Essentially-non-oscillatory reconstruction

If the discrete stencil defining $\tilde{u}_{\text{opt}}(x)$ contains a discontinuity or large gradients, spurious oscillations can appear in the numerical solution. To avoid such a problem we construct a WENO procedure that smoothly adapts the stencil in the neighbourhood of the singularity.

Defining the non-oscillatory reconstruction on I_i by $\tilde{u}_i(x)$, we want the following properties to be verified:

$$\tilde{u}_i(x) = \begin{cases} \tilde{u}_{\text{opt}}(x) & \text{if the stencil } \{I_{i-1}, I_i, I_{i+1}\} \text{ is in the smooth regions} \\ \tilde{u}_1(x) & \text{if the solution is not smooth and } \{I_{i-1}, I_i\} \text{ is in the smooth region} \\ \tilde{u}_2(x) & \text{if the solution is not smooth and } \{I_i, I_{i+1}\} \text{ is in the smooth region} \\ \bar{u}_i, & \text{otherwise} \end{cases} \tag{14}$$

The latter condition is specific to a Hermite interpolation.

Indeed, this condition becomes necessary when the solution is discontinuous and the central point of the stencil $\{I_{i-1}, I_i, I_{i+1}\}$ is such that

$$\bar{r}_i = \mathrm{O}\left(\frac{1}{\Delta x}\right) \tag{15}$$

In such a case, the property (15) may introduce an oscillation $\mathrm{O}(1/\Delta x)$ into the interpolation; consequently, neither the stencil $\{I_{i-1}, I_i\}$ nor the stencil $\{I_i, I_{i+1}\}$ that use $\bar{r}_i$ are admissible to generate a non-oscillatory reconstruction. The solution adopted to circumvent this problem is to locally degrade the scheme with the first-order when the property (15) appears.

At least theoretically, this new characteristic could be estimated as a drawback when compared with classical finite-volume WENO schemes. However, one can make two remarks to moderate this point:

- Owing to the property of convexity of physical flux, characteristic curves converge towards the shock wave when this one exists. This means that the numerical error generated in discretizing such a discontinuity remains confined near this one. Unfortunately, this is no more the case when a linear discontinuity such as a contact discontinuity, appears into the solution: in such a case one can expect this discontinuity to be under solved.
- As demonstrated in [14] or [15], all shock-capturing methods satisfy, at best, the Rankine–Hugoniot jump conditions to first-order in L_1-norm, regardless of how accurately they model the differential equations.

To implement a specific solution technique, we extended the principle of the central WENO interpolation defined in [12].

First, we construct an ENO interpolant as a combination of Hermite polynomials that are based on different discrete stencils.

Specifically, we define in the discrete cell I_i:

$$\tilde{u}_i(x) \equiv \bar{u}_i + \sum_j w_j(\tilde{u}_j(x) - \bar{u}_i), \quad w_j \geqslant 0, \ \ j \in \{1, 2, c\}, \tag{16}$$

where $\tilde{u}_1(x)$ (resp. $\tilde{u}_2(x)$) is the third-degree polynomial based on the left stencil $\{I_{i-1}, I_i\}$ (resp. right stencil $\{I_i, I_{i+1}\}$) and $\tilde{u}_c(x)$ is a fifth-degree central polynomial.

Consequently, upon considering (16), all that is left is to reconstruct a central polynomial, $\tilde{u}_c(x)$, such that the combination, (16), will be sixth-order accurate in smooth regions. In other words, $\tilde{u}_c(x)$ must be such that $\tilde{u}_i(x) \approx \tilde{u}_{\text{opt}}(x)$ in smooth regions.

Therefore, it must verify

$$\begin{aligned} &\tilde{u}_{\text{opt}}(x) = \bar{u}_i + C_1 \times (\tilde{u}_1(x) - \bar{u}_i) + C_2 \times (\tilde{u}_2(x) - \bar{u}_i) + C_c \times (\tilde{u}_c(x) - \bar{u}_i) \quad \forall x \in I_i \\ &\sum_j C_j = 1, \quad C_j \geqslant 0, \qquad j \in \{1, 2, c\} \end{aligned} \tag{17}$$

The constants C_j represent ideal weights so that $\tilde{u}_i(x)$ is identified with $\tilde{u}_{\text{opt}}(x)$ when the solution is smooth. As already noted in [12], the freedom in selecting those constants has no influence on the properties of the numerical stencil; any symmetric choice in (17), provides the desired accuracy for $\tilde{u}_{\text{opt}}(x)$.

In what follows, we make the choice: $C_1 = C_2 = 1/4$, $C_c = 1/2$. Then, the central polynomial, $\tilde{u}_c(x)$, can be deduced from (17):

$$\tilde{u}_c(x) = \bar{u}_i + [(\tilde{u}_{\text{opt}}(x) - \bar{u}_i) - C_1(\tilde{u}_1(x) - \bar{u}_i) - C_2(\tilde{u}_2(x) - \bar{u}_i)]/C_c \quad \forall x \in I_i \tag{18}$$

The role of $\tilde{u}_c(x)$ is only to get an optimal accuracy in smooth regions; in the presence of a discontinuity, the weights of $\tilde{u}_c(x)$ and one of the left or the right stencil will be practically zero; then, the remaining one-sided stencil that lies in the smooth region, will provide a fourth-order non-oscillatory reconstruction of the solution.

To complete the reconstruction of $\tilde{u}_i(x)$ and to ensure properties (14), it is left to compute the weights, w_j. To define those weights, we follow the reasoning of [2].

To achieve the optimal interpolation, (17), in smooth regions, the weights w_j must smoothly converge to the ideal weights C_j as Δx approaches zero. In an opposite way, in regions where a discontinuity does exist, the weights should effectively remove the contribution of stencils that contain the discontinuity, according to properties (14).

To this end, combining (16) and (17) gives

$$\tilde{u}_i(x) = \tilde{u}_{\text{opt}}(x) + \sum_{j\in\{1,2,c\}} (w_j - C_j)(\tilde{u}_j(x) - \bar{u}_i) \quad \forall x \in I_i \tag{19}$$

Since $\tilde{u}_j(x) = u(x) + \mathrm{O}(\Delta x^4)$, $j \in \{1,2,c\}$, wherever the solution is smooth, (19) can be re-written as

$$\tilde{u}_i(x) = \tilde{u}_{\text{opt}}(x) + \sum_{j\in\{1,2,c\}} (w_j - C_j)(u(x) - \bar{u}_i + D_j\Delta x^4) \quad \forall x \in I_i \tag{20}$$

Therefore, the second term of (20) must be at least an $\mathrm{O}(\Delta x^6)$ quantity in order for the combination to be sixth-order accurate at the boundary extrapolated points.

Then, sufficient conditions are

$$\begin{cases} \left(\sum\limits_{j\in\{1,2,c\}} w_j - 1\right)(u(x) - \bar{u}_i) = \mathrm{O}(\Delta x^6) \\ \sum\limits_{j\in\{1,2,c\}} (w_j - C_j)D_j = \mathrm{O}(\Delta x^2) \end{cases} \tag{21}$$

But, since $(u(x) - \bar{u}_i) = \mathrm{O}(\Delta x)$, it is sufficient to require

$$\begin{cases} \sum\limits_{j\in\{1,2,c\}} w_j - 1 \leqslant \mathrm{O}(\Delta x^5) \\ w_j - C_j \leqslant \mathrm{O}(\Delta x^2), w_j \geqslant 0 \quad \forall j \in \{1,2,c\} \end{cases} \tag{22}$$

Up to this point, the development of the sixth-order Hermite WENO scheme has been general. To fully determine the HCWENO6 scheme, we need now to specify the nonlinear weights. Before that, note that constraints presented in [2] ($\sum_j w_j = 1, w_j \in [0,1]$) are slightly more restrictive than (22). In our case, the condition given in [2] must be relaxed in order for the scheme to entirely complete properties (14). This means that the nonlinear weights designed in [2] cannot ensure the ENO property of (16): specific weights must be formulated to retain sixth-order convergence properties and to avoid Gibbs-like phenomena near discontinuities.

3.3. The nonlinear weights

To begin, we calculate the general indicators of smoothness defined in [2]

$$\mathrm{IS}_j^i \equiv \frac{1}{u_{\max}^2} \sum_k \Delta x_i^{2k-1} \times \int_{I_i} \left(\frac{\mathrm{d}^k \tilde{u}_j}{\mathrm{d}x^k}\right)^2 \mathrm{d}x, \quad j \in \{1,2,c\} \tag{23}$$

where $u_{\max}$ is calculated over the whole calculation domain Ω: $u_{\max} = \max|u|_{x\in\Omega}$. Those indicators provide a measure of the smoothness of the solution over the cell I_i, according to the particular stencil selected to define $\tilde{u}_j(x)$ on that cell.

In regions of smoothness, $IS_j^i \ll 1$, whereas $IS_j^i = O(1)$ in cells with strong gradients or discontinuities.

Specifically, formula (23) can be explicited for $\tilde{u}_1(x)$ and $\tilde{u}_2(x)$ ($\equiv \sum_{j=1}^{4} a_{j-1}x^{j-1}$) on a non-uniform mesh:

$$IS_j^i = a_1^2\Delta x_i^2 + \left(\frac{13}{3}a_2^2 + \frac{1}{2}a_1a_3\right)\Delta x_i^4 + \frac{3129}{80}a_3^2\Delta x_i^6, \quad j \in \{1,2\} \tag{24}$$

For $\tilde{u}_c(x)$, formula (23) and result (18) give

$$IS_c^i = a_1^2\Delta x_i^2 + \left(\frac{13}{3}a_2^2 + \frac{1}{2}a_1a_3\right)\Delta x_i^4 + \left(\frac{1}{8}a_1a_5 + \frac{21}{5}a_2a_4 + \frac{3129}{80}a_3^2\right)\Delta x_i^6 \tag{25}$$

The polynomial coefficients $\{a_j\}$ are calculated by numerically inverting (11).

Hence, having calculated IS_j^i, we introduce the new sensor, β_j^i, $j \in \{1,2,c\}$, a normalized smoothness indicator defined on I_i and such that

$$\begin{cases} \beta_j^i \to 0 \text{ in regions of smoothness} \\ \beta_j^i \to 1 \text{ if there exist a discontinuity} \end{cases} \tag{26}$$

Practically, we suggest the following formulation for this sensor:

$$\beta_j^i \equiv \frac{(IS_j^i)^2}{1 + (IS_j^i)^2}, \quad j \in \{1,2,c\} \quad \forall x \in I_i \tag{27}$$

From the asymptotic behaviour of the smoothness indicator and depending on the smoothness of the solution, IS_j^i, one can easily verify that formulation (27) follows the requirements of (26).

By normalizing the domain of variation of the smoothness indicator, such a formulation makes it possible to define more easily smooth functions for the calculation of the nonlinear weights, w_j. Moreover, this normalized smoothness indicator prevents the use of the parameter ε that appears in [2]. Indeed, this parameter was initially introduced to prevent an indeterminate form in the calculation of the w_j. However, as demonstrated in [16], this parameter plays a crucial role and must be selected on a case-by-case basis since it appears as a dimensional quantity.

After several trials and errors with the numerical experiments presented below, we propose the following formulation to calculate the weights w_j on I_i:

$$w_j \equiv \frac{C_j}{2}\left[1 + \tanh\left(\frac{1 - 4(\beta_j^i)^2}{2\mu}\right)\right], \quad j \in \{1,2,c\} \tag{28}$$

μ is non-dimensionalized parameter introduced to adjust the switch between the ideal weights, C_j, defined in (17) and the ENO weights. Extensive numerical computations have shown that the best compromise between accuracy and non-oscillatory properties was ensured for $\mu = 0.1$. Practically, this parameter will remain unchanged in what follows.

When the mesh is uniform, one can verify the validity of (28). Indeed, expansions of (24) and (25) around $x = x_i$ ($\Delta x_i \equiv Cte \equiv \Delta x$), yield the following results:

$$IS_j^i = (\Delta x \times u_x)^2 + \frac{13}{12}(\Delta x^2 u_{xx})^2 + O(\Delta x^5), \quad j \in \{1,2,c\} \tag{29}$$

Therefore, the IS_j^i are of the form:

$$IS_j^i = (\Delta x \times u_x)^2(1 + C\Delta x^2), \quad j \in \{1,2,c\} \tag{30}$$

Consequently, the β_j^i are such that

$$\beta_j^i \approx \frac{(\Delta x \times u_x)^4}{1 + (\Delta x \times u_x)^4} \tag{31}$$

Thus $\beta_j^i = \mathrm{O}(\Delta x^4)$ in regions of smoothness and approaches unity by its lower bound in the cells crossed by a discontinuity.

Finally, by expanding (28) around $\beta_j^i \equiv 0$ and $\beta_j^i \equiv 1$, one can deduce the following asymptotic behaviour for the w_j:

$$w_j \approx \begin{cases} C_j\left[1 - \frac{4e^{\frac{1}{\mu}}}{(1+e^{\frac{1}{\mu}})^2 \times \mu}\Delta x^8\right] & \text{if } \beta_j^i = \mathrm{O}(\Delta x^4) \\ C_j\left[\frac{-8e^{\frac{-3}{\mu}}}{(e^{\frac{-3}{\mu}}+1)^2 \times \mu} \times (\beta_j^i - 1)\right] & \text{if } \beta_j^i \to 1^- \end{cases} \tag{32}$$

One can check that conditions (22) are satisfied provided that $\mu \ll 1$. Moreover, the convergence of w_j towards the ideal weights is very fast when $\beta_j^i \ll 1$. Indeed, with the value $\mu = 0.1$, we get from (32) the following result:

$$w_j = C_j(1 - 1.8 \times 10^{-3}(\beta_j^i)^2 + \mathrm{O}[(\beta_j^i)^3]) \tag{33}$$

Similarly, when β_j^i approaches unity, we obtain

$$w_j = C_j(-7.5 \times 10^{-12}(\beta_j^i - 1) + \mathrm{O}[(\beta_j^i - 1)^2]) \tag{34}$$

This fast rate of convergence is an advantage since it means that the region of low precision will be circumscribed around the singularity.

Practically, to reach machine precision, w_j is set to the ideal weight, C_j, as soon as $|w_j - C_j| \leqslant 10^{-3}$ in a cell. Similarly, w_j is set to zero when the coefficient in front of C_j in (28) is lower than 10^{-8}. Those values were optimized by considering the Burgers equation. Although such a procedure introduces new parameters into the method – parameters that may be problem dependent – all the numerical results presented in this article are computed with the same thresholds for all the test cases investigated.

3.4. The HCWENO6 upwind scheme for scalar hyperbolic problems

The final form of the HCWENO6 upwind scheme is given by

$$\begin{cases} \left.\frac{\partial f}{\partial x}\right|_i = \frac{(\tilde{f}_{i+1/2} - \tilde{f}_{i-1/2})}{\Delta x_i} \\ \left.\frac{\partial g}{\partial x}\right|_i = \frac{(\tilde{g}_{i+1/2} - \tilde{g}_{i-1/2})}{\Delta x_i} \end{cases} \tag{35}$$

and

$$\begin{cases} \tilde{u}_{i+1/2}^{\mathrm{L}} = \bar{u}_i + \sum\limits_{j\in\{1,2,c\}} w_j \times (\tilde{u}_j(x_{i+1/2}) - \bar{u}_i) \\ \tilde{r}_{i+1/2}^{\mathrm{L}} = \bar{r}_i + \sum\limits_{j\in\{1,2,c\}} w_j \times \left(\frac{\mathrm{d}}{\mathrm{d}x}\tilde{u}_j(x_{i+1/2}) - \bar{r}_i\right) \end{cases} \tag{36}$$

Contrarily to [10], the same Hermite polynomial is used to interpolate both the function $(\tilde{u}_{i+1/2}^{\mathrm{L}})$ and its derivative $(\tilde{r}_{i+1/2}^{\mathrm{L}})$; this means that the nonlinear weights are unchanged when passing from $\tilde{u}_{i+1/2}^{\mathrm{L}}$ to $\tilde{r}_{i+1/2}^{\mathrm{L}}$.

$\tilde{f}_{i+1/2}$ and $\tilde{g}_{i+1/2}$ are calculated by the HLL solver (formulae (5) and (6)). The nonlinear weights, $\{w_j\}$, are given by equation (28) and calculated from (24), (25) and (27). The polynomial coefficients, $\{a_j\}$, used in (24) and (25) are calculated by numerically inverting three linear systems such as (11): two 4×4 systems for the coefficients of $\tilde{u}_j(x), j \in \{1,2\}$ and a 6×6 system for $\tilde{u}_{\mathrm{opt}}(x)$: $\tilde{u}_c(x)$ is then deduced from those polynomials (formula (18)). Then, the calculation of $(\tilde{u}_{i+1/2}^{\mathrm{L}}, \tilde{r}_{i+1/2}^{\mathrm{L}})$ can be done by using (12) for each polynomial.

3.5. Extension to nonlinear systems: the one-dimensional Euler equations

In this section, we extend the HCWENO6 scheme to solve systems of hyperbolic conservation laws. Specifically, we consider the one-dimensional Euler equations in the following conservation form:

$$\frac{\partial \mathbf{U}}{\partial t} + \frac{\partial \mathbf{F}(U)}{\partial x} = 0 \tag{37}$$

where

$$\mathbf{U} \equiv [\rho, \rho u, \rho E]^t, \quad \mathbf{F} \equiv [\rho u, \rho u^2 + p, \rho u H]^t \tag{38}$$

$H \equiv E + p/\rho$ is the specific total enthalpy and this set of equations is closed by the equation-of-state of an ideal gas: $p = (\gamma - 1)(\rho E - u^2/2)$, $\gamma = 1.40$.

To use a Hermite procedure, we derive the following set of systems from (37):

$$\begin{cases} \dfrac{\partial \mathbf{U}}{\partial t} + \dfrac{\partial \mathbf{F}(U)}{\partial x} = 0 \\ \dfrac{\partial \mathbf{V}}{\partial t} + \dfrac{\partial \mathbf{G}(U,V)}{\partial x} = 0 \end{cases} \tag{39}$$

where we defined $\mathbf{V} \equiv [(\rho)_x, (\rho u)_x, (\rho E)_x]^t$, $\mathbf{G} \equiv [(\rho u)_x, (\rho u^2 + p)_x, (\rho u H)_x]^t$.

As in the scalar case, the semi-discrete conservative finite-volume scheme discretizing (39) is then written as

$$\begin{cases} \frac{\mathrm{d}\overline{\mathbf{U}}_i}{\mathrm{d}t} = -\frac{1}{\Delta x_i}[\widetilde{\mathbf{F}}_{i+1/2} - \widetilde{\mathbf{F}}_{i-1/2}] \\ \frac{\mathrm{d}\overline{\mathbf{V}}_i}{\mathrm{d}t} = -\frac{1}{\Delta x_i}[\widetilde{\mathbf{G}}_{i+1/2} - \widetilde{\mathbf{G}}_{i-1/2}] \end{cases} \tag{40}$$

To calculate $(\widetilde{\mathbf{F}}_{i+1/2}, \widetilde{\mathbf{G}}_{i+1/2})$, the HLL solver defined in the scalar case by (5) and (6), is simply extended to the case of the Euler equations by re-defining the characteristic velocities $\lambda^{\pm}_{i+1/2}$:

$$\begin{cases} \lambda^{+}_{i+1/2} \equiv \max(u^{\mathrm{L}}_{i+1/2} + a^{\mathrm{L}}_{i+1/2}, u^{\mathrm{R}}_{i+1/2} + a^{\mathrm{R}}_{i+1/2}, 0) \\ \lambda^{-}_{i+1/2} \equiv \min(u^{\mathrm{L}}_{i+1/2} - a^{\mathrm{L}}_{i+1/2}, u^{\mathrm{R}}_{i+1/2} - a^{\mathrm{R}}_{i+1/2}, 0) \end{cases} \tag{41}$$

where $a^{\mathrm{L,R}} \equiv \left.\sqrt{\frac{\gamma p}{\rho}}\right|^{\mathrm{L,R}}$ is the speed of sound for an ideal gas.

The conservative point-values, $(\mathbf{U}^{\mathrm{L,R}}_{i+1/2}, \mathbf{V}^{\mathrm{L,R}}_{i+1/2})$, are calculated from the interpolated primitive variables $[\rho^{\mathrm{L,R}}_{i+1/2}, u^{\mathrm{L,R}}_{i+1/2}, p^{\mathrm{L,R}}_{i+1/2}]^t$ and $[(\rho_x)^{\mathrm{L,R}}_{i+1/2}, (u_x)^{\mathrm{L,R}}_{i+1/2}, (p_x)^{\mathrm{L,R}}_{i+1/2}]^t$. Those variables are interpolated by using the HCWENO6 procedure developed in the scalar case. Although this choice is not referenced in the literature as the best one for dealing with one-dimensional problems (a characteristic-wise reconstruction would be more suitable) it has the advantage of being general since its extension to multi-dimensional problems is straightforward. This is no more the case if one selects the characteristic variables since those quantities are undefined (there exists an infinite number of characteristic directions for a multi-dimensional hyperbolic problem). Let us note however, that the characteristic directions selected for multi-dimensional computations, can be grid aligned; such a choice may give good numerical results but its justification becomes then of empirical nature so that a characteristic-wise reconstruction can be considered, a priori, equivalent to a component-wise reconstruction.

Lastly, only one smoothness indicator is calculated for the all the variables of the problem; this indicator is based upon the density, ρ, since this quantity detects both a shock and a contact discontinuity.

We ensure the time-integration of (40) by using the third-order TVD Runge–Kutta procedure defined by (9).

4. Numerical validation

4.1. Asymptotic stability analysis

To begin, we study the asymptotic stability of the HCWENO6 scheme. To this end, we compute the complex eigenvalues of the matrices obtained by the spatial discretization of the following scalar linear system:

$$\begin{cases} u_t + u_x = -\frac{1}{S}\frac{\mathrm{d}S}{\mathrm{d}x}u \quad \forall x \in [0,1] \\ r_t + r_x = -\frac{\mathrm{d}}{\mathrm{d}x}\left(\frac{1}{S}\frac{\mathrm{d}S}{\mathrm{d}x}\right)u - \frac{1}{S}\frac{\mathrm{d}S}{\mathrm{d}x}r, \quad (r \equiv u_x) \end{cases} + \begin{cases} u(x=0,t) = f(t) \\ u(x=0,t) = g(t) \end{cases} \tag{42}$$

The computational domain is divided into N non-uniform intervals of width Δx_i ($\equiv x_{i+1/2} - x_{i-1/2}$). The spatial derivatives at all grid points, including the boundary points, are discretized by using the algebraic formulae

previously developed. In such a case, we use the algebraic formulae defining the optimal polynomial and the points close to the boundary are discretized with the same accuracy (sixth-order) as the interior points.

The source term: $-\frac{1}{S}\frac{\mathrm{d}S}{\mathrm{d}x}u$, is introduced to model problems with a varying geometry according to x (for example, the one-dimensional nozzle flow problem).

In our example, the shape of the geometry is given by $S(x) \equiv x^2 - x + 1/2$.

Thus, we write the upwind approximations:

$$\begin{cases} u_x|_i \approx \frac{u^{\mathrm{L}}_{i+1/2} - u^{\mathrm{L}}_{i-1/2}}{\Delta x_i} \\ r_x|_i \approx \frac{r^{\mathrm{L}}_{i+1/2} - r^{\mathrm{L}}_{i-1/2}}{\Delta x_i} \end{cases} \tag{43}$$

Substituting the approximation (43) into the linear system (42) with the Dirichlet boundary conditions such as defined in (42), leads to a system of ODEs that can be written

$$\frac{\mathrm{d}\mathbf{U}}{\mathrm{d}t} = \mathbf{M}\mathbf{U} + \mathbf{Q}_u f(t) + \mathbf{Q}_r g(t) + \mathbf{S}\mathbf{U} \tag{44}$$

where $\mathbf{U} \equiv [\bar{u}_i, \bar{r}_i]^t$ is a $2N$-dimensional vector representing the values of the solution and its derivatives at the discrete points.

$\mathbf{M}$ is a $2N \times 2N$ matrix that contains the algebraic coefficients for the discretization and $\mathbf{S}$ the $2N \times 2N$ matrix accounting for the source terms. Lastly, $\mathbf{Q}_u$ and $\mathbf{Q}_r$ are vectors of dimension $2N$ accounting for the boundary conditions at $x = 0$.

The asymptotic stability condition for the semi-discrete system (44) is that all eigenvalues of matrix $\mathbf{M} + \mathbf{S}$ only contain negative real parts. This is a necessary but not sufficient condition for the stability of long-time-integration of the system, [18].

To begin, we study the spatial discretization of (42) with $\mathbf{S} \equiv 0$ (no source terms). Fig. 3 gives numerical results for $N = 100$ and $N = 200$ grid points and for two grid stretching typified by $\Delta x_{\min}/\Delta x_{\max} = 1$ (uniform grid) and $\Delta x_{\min}/\Delta x_{\max} = 0.1$ (stretched grid). As expected, the upwinded space operator generates eigenvalues of which the real component is different from zero: this real component indicates that the space discretization operator has generated numerical dissipation. As one can see, the discretization is stable and is free of the grid stretching: the eigenvalue which is closest to the unstable area is such that $\mathrm{Re}(\lambda) = 10^{-16}$, $\mathrm{Im}(\lambda) = 0$, whatever the stretching of the grid or the mesh resolution, Fig. 3(a)–(d). However, this is not always true. Indeed, when a source term is introduced the real part of the discrete eigenvalues is not everywhere strictly negative, Fig. 4. This is especially true for a grid stretching $\Delta x_{\min}/\Delta x_{\max} = 0.1$ (the mesh is refined in the zone where $\mathbf{S}$ is minimum), since more than 200 grid points are necessary in order for the largest real part of the discrete eigenvalues to be zero at the machine precision (10^{-8} in simple precision).

This means that the amount of stretching required for stability is a function of the number of grid points when a source term is introduced in the equations. Practically, the computation of such problems is expected to be more difficult.

Now, we study the time-integration of (44) by the third-order Runge–Kutta TVD procedure (9). For those computations, the CFL is selected such that $\Delta t/\min_i(\Delta x_i) = 0.8$. First, Fig. 5 presents numerical results with no source terms ($\mathbf{S} \equiv 0$ in (44)). As one can see, the HCWENO6 scheme with Dirichlet boundary conditions is stable even on stretched meshes, since the discrete eigenvalue spectrum lies in the stability area of the Runge–Kutta scheme. However, when one increases the CFL number to 0.9, some discrete eigenvalues are outside the stability region: the numerical scheme then becomes unstable.

Now, if we introduce a source term in (44), we get the results presented in Fig. 6. We can see that with a sufficient grid resolution ($N = 250$, $\mathrm{CFL} = 0.8$), the scheme remains stable, even if the mesh is stretched ($\Delta x_{\min}/\Delta x_{\max} = 0.1$).

To conclude this fist study, one can say that the discretization of the spatial term by the sixth-order Hermite interpolation, is free of the grid stretching as long as there is no source term. When a source term exists, the mesh resolution must be carefully selected; this is especially true when the source is highly varying. Moreover, the influence of the boundary conditions imposes a practical limit to the CFL number.

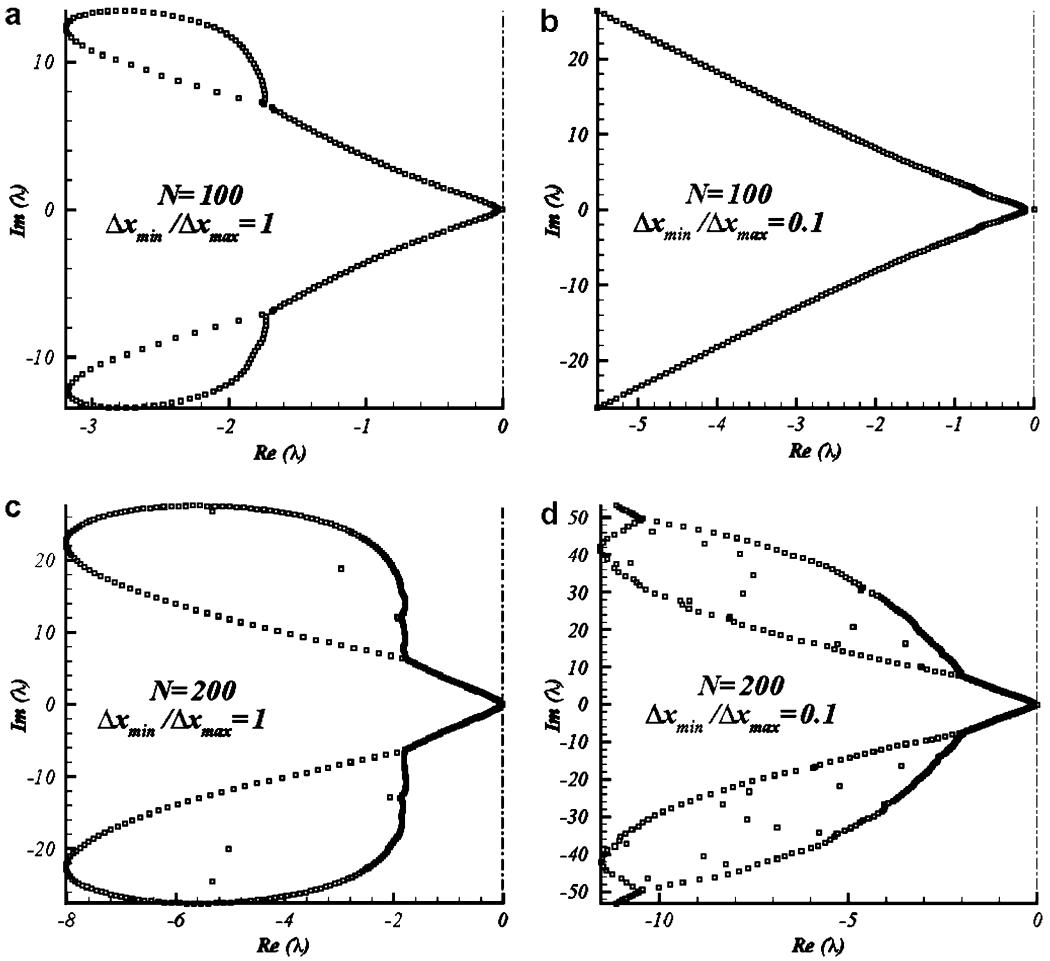

Fig. 3. Asymptotic stability analysis: eigenvalue spectra for the discretization of u_x by the HCWENO6 scheme. Influence of the grid stretching, $\Delta x_{\min}/\Delta x_{\max}$ and the grid resolution, N.

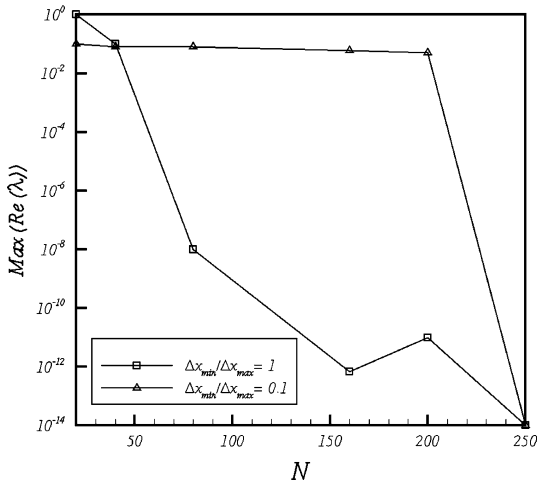

Fig. 4. Asymptotic stability analysis. Largest real part of the discrete spectra for the discretization of $u_x + \frac{1}{S}\frac{dS}{dx}u$ by the HCWENO6 scheme. Influence of the mesh resolution, N, for a given stretching of the grid, $\Delta x_{\min}/\Delta x_{\max}$.

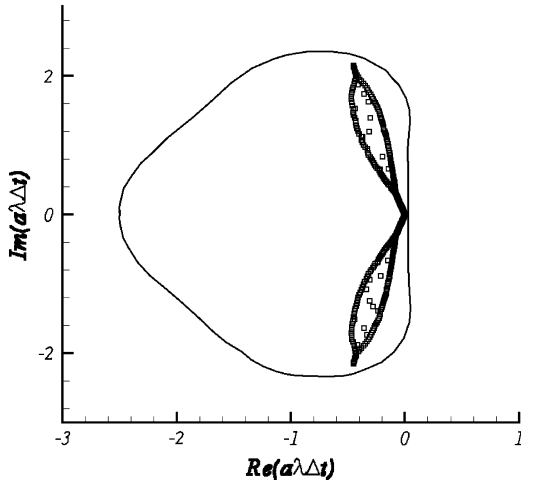

Fig. 5. Space–time discretization of $u_t + u_x = 0$. $N = 200$, $\Delta x_{\min}/\Delta x_{\max} = 0.1$, CFL = 0.8.

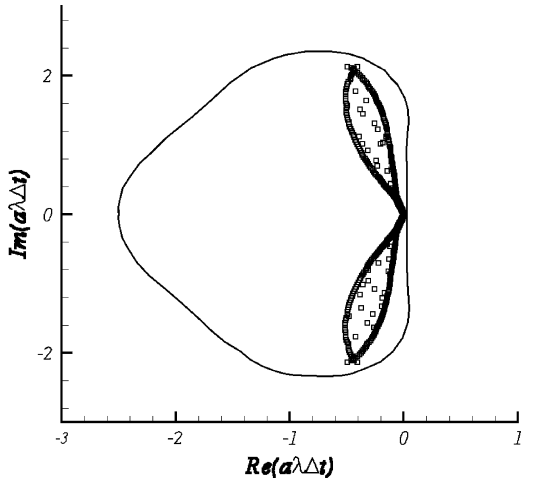

Fig. 6. Space–time discretization of $u_t + u_x = -\frac{1}{S}\frac{dS}{dx}u$ $N = 250, \Delta x_{\min}/\Delta x_{\max} = 0.1$, CFL = 0.8.

4.2. Nonlinear scalar problem: the Burgers equation

We solve the following nonlinear scalar Burgers equation:

$$u_t + \left(\frac{u^2}{2}\right)_x = 0 \quad \forall x \in [0,2] \tag{45}$$

with the initial condition: $u(x, t = 0) = 1/2 + \sin(\pi x)$ and a 2-periodic boundary condition. To begin, a uniform mesh with N cells is used for this test case. The CFL number is defined as $\max_i|u_i^n|\Delta t/\min_i \Delta x_i$. Its value is taken as 0.5 for both HCWENO6 and HUWENO5 schemes. For the accuracy tests, since the time-integration method incurs $O(\Delta t^3)$ errors, the time step is chosen to be $\Delta t = \Delta x^2/2$ for the HCWENO6 scheme in order for the discretization error of the overall scheme to be a measure of the spatial convergence only. The same scaling for the time step is selected for the HUWENO5 scheme.

When $t = 1/2\pi$, the solution is still smooth and the discrete errors and numerical orders of accuracy are shown in Table 1 (HCWENO6 scheme) and Table 2 (HUWENO5 scheme). As can be seen, both schemes reach their designed order of accuracy; however, the HCWENO6 produces a lower error level on the same

Table 1
$u_t + uu_x = 0$; $u(x, t = 0) = 1/2 + \sin(\pi \times x)$; HCWENO6 scheme with periodic boundary conditions; $t = 1/2\pi$; $\Delta t = \Delta x^2/2$; L_1 and L_∞ errors

N	L_1 error	L_1 order	L_∞ error	L_∞ order
10	2.51×10^{-4}	–	5.81×10^{-4}	–
20	3.18×10^{-5}	3	1.42×10^{-4}	2
40	9.36×10^{-7}	5.1	6.03×10^{-6}	4.6
80	2.14×10^{-8}	5.4	1.57×10^{-7}	5.3
160	4.20×10^{-10}	5.7	3.47×10^{-9}	5.5
320	7.30×10^{-12}	5.9	6.18×10^{-11}	5.8

Table 2
$u_t + uu_x = 0$; $u(x, t = 0) = 1/2 + \sin(\pi \times x)$; HUWENO5 scheme with periodic boundary conditions; $t = 1/2\pi$; $\Delta t = \Delta x^2/2$; L_1 and L_∞ errors

N	L_1 error	L_1 order	L_∞ error	L_∞ order
10	3.66×10^{-3}	–	7.29×10^{-3}	–
20	1.86×10^{-4}	4.1	8.03×10^{-4}	3
40	1.07×10^{-5}	3.9	6.06×10^{-5}	3.5
80	3.54×10^{-7}	4.9	2.73×10^{-6}	4.5
160	1.20×10^{-8}	4.9	9.27×10^{-8}	4.9
320	3.80×10^{-10}	5	3×10^{-9}	5

mesh. Fig. 7 explains this result: we compare the nonlinear weights for the HCWENO6 and the HUWENO5 schemes ($N = 80$ grid points). We can see that the nonlinear weights have everywhere their ideal values for the HCWENO6 scheme; this is no more the case if one considers the HUWENO5 scheme, although the solution remains smooth. When $t = 3/2\pi$, a shock has already appeared in the solution and it is located at $x = 1.238$.

Fig. 8 shows the numerical solution on two meshes: a uniform mesh with $N = 80$ grid points, Fig. 8(a), and a stretched mesh near the shock place ($\Delta x_{\min}/\Delta x_{\max} = 0.1$), Fig. 8(b). As one can note it, the shock is captured without any numerical oscillation in both cases. In Fig. 9, we compare this result with the HUWENO5 scheme on a uniform mesh: in both cases, the shock is captured in the same way though those schemes are structurally very different. However, the HCWENO6 scheme produces a lower discretization error in the smooth regions, Fig. 9(b).

Lastly, Fig. 10 compares the nonlinear weights for both schemes; in what concerns the HCWENO scheme, it is interesting to note that the three weights are zero ($w_1 = w_2 = w_c = 0$) at the nearest point of the shock region ($x = 1.238$): this means that the scheme becomes, locally, a first-order scheme. However, as already mentioned, this approximation remains local and does not alter the global solution, Fig. 9(b).

4.3. One-dimensional hyperbolic systems: the Euler equations

Unless mentioned, the computations are run on a uniform mesh ($\Delta x_i \equiv Cte$). N grid points are utilized to discretize the equations.

The CFL number is defined as

$$\mathrm{CFL} \equiv \Delta t \times \frac{\max_i(|u_i| + a_i)}{\min_i \Delta x_i}$$

We choose CFL = 0.5 for almost all test cases, except for the accuracy tests.

Example 1. We solve the Euler equations, (37), in the domain $[0, 2]$. The initial condition is set to be: $\rho(x, t = 0) = 1 + 0.2 \times \sin(\pi x)$, $u(x, t = 0) = 1$, $p(x, t = 0) = 1$, with a 2-periodic boundary condition. The numerical solution is computed up to $t = 2$ with $\Delta t = \mathrm{O}(\Delta x^2)$ (HCWENO6 and HUWENO5 schemes). The errors and numerical orders of accuracy of the density, ρ, for the HCWENO6 scheme (resp. HUWENO5

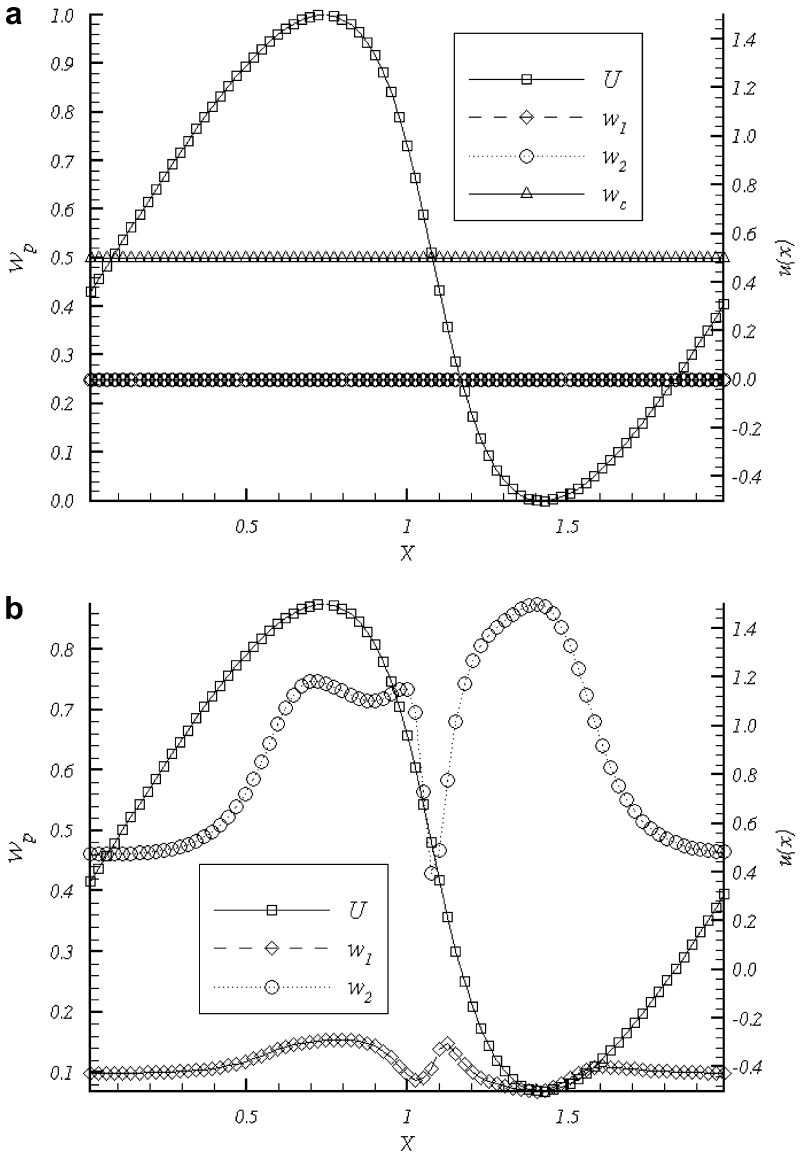

Fig. 7. Burgers equation. $u(x,t=0)=1/2+\sin(\pi x)$, $t=1/2\pi$, $N=80$, CFL $=0.01$. Nonlinear weights: (a) HCWENO6 scheme, (b) HUWENO5 scheme.

scheme) are shown in Table 3 (resp. Table 4). Both schemes reach their theoretical order of accuracy and the HCWENO6 remains the most accurate one.

Example 2 (*Lax problem*).
This problem only contains shocks and simple smooth region solutions. It is simply used to demonstrate the non-oscillatory properties of the HCWENO6 scheme near discontinuities and to validate the specific choices made for the indicators of smoothness.

The Lax problem is defined by the following left- and right-initial states

$$(\rho,u,p)^{\mathrm{L}}=(0.445,0698,3.528)\quad \forall x\leqslant 0,\qquad (\rho,u,p)^{\mathrm{R}}=(0.5,0,0.571)\quad \forall x>0$$

100 grid points are used to discretize the computational domain $[0,1]$. The solution is run up to $t=1.30$.

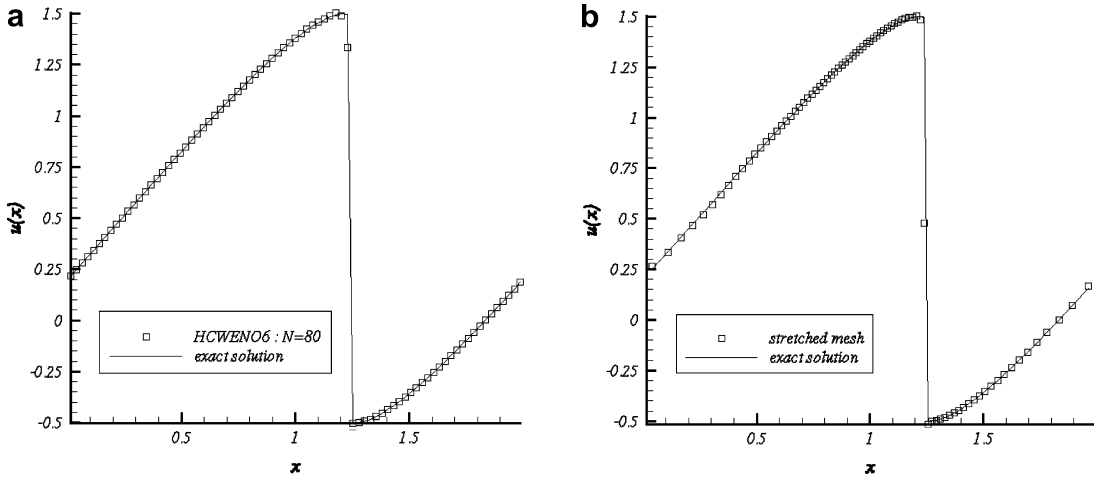

Fig. 8. Burgers equation. $u(x,t=0)=1/2+\sin(\pi x)$, $t=3/2\pi$, $N=80$, CFL $=0.5$. HCWENO6 scheme: (a) uniform mesh, (b) non-uniform mesh ($\Delta x_{\min}/\Delta x_{\max}=0.1$).

Although this problem is not necessarily a good test for high-order shock-capturing schemes (a good second-order ENO scheme would suffice, see [1] for example), we can see that the HCWENO6 scheme performs reasonably well, Fig. 11. The contact discontinuity is smeared more than the shock, Fig. 11(a). As expected, the component-wise reconstruction is oscillatory; this is clearly visible in the velocity profile, Fig. 11(c). Those oscillations become less significant when the mesh is refined. It should however be pointed out that these oscillations are less "noisy" than more classical component-wise reconstructions such as the ENO scheme, [1] or the CWENO scheme, [23].

Therefore, it appears that the single density is a well adapted sensor for computing the smoothness indicators for all components.

Example 3 (*Interacting blast waves*, [24]). We solve the Euler equations, (37), with initial conditions

$$(\rho,u,p)=\begin{cases}(1,0,10^{3}) & \forall x\in[0,0.1[\\ (1,0,10^{-2}) & \forall x\in[0.1,0.9[\\ (1,0,10^{2}) & \forall x\in[0.9,1]\end{cases}$$

A reflective boundary condition is applied at both $x=0$ and $x=1$.

The computed density ρ is plotted at $t=0.038$ against the "exact" solution; this solution is a converged solution computed by a classical second-order TVD scheme ("minmod" limiter) with 3000 grid points.

In Fig. 12, we show the numerical results of the HCWENO6 scheme with $N=200$ grid points (Fig. 12(a)) and $N=300$ grid points (Fig. 12(b)).

We can see that the $N=200$ results give reasonably good results although some oscillations appear behind the first contact discontinuity, near $x=0.70$. This solution is improved with the $N=300$ results (Fig. 12(b)): the three contact waves, near $x=0.59,0.76,0.80$, are better predicted. In such a case, the HCWENO6 scheme resolves the salient features of the flow with a good fidelity.

Example 4 (*Shock entropy wave interactions*, [2]). This problem is very suitable for high-order shock-capturing schemes because both shocks and complicate smooth flow features co-exist. In this example, a moving shock interacts with an entropy wave of small amplitude.

On the domain $[0,5]$, the initial condition is the following:

$$(\rho,u,p)=(3.857143,2.629369,10.333333)\quad \forall x<1/2$$
$$(\rho,u,p)=(\mathrm{e}^{-\varepsilon\sin(kx)},0,1)\quad \forall x\geqslant 1/2$$

where ε and k are the amplitude and the wave number of the entropy wave, respectively.

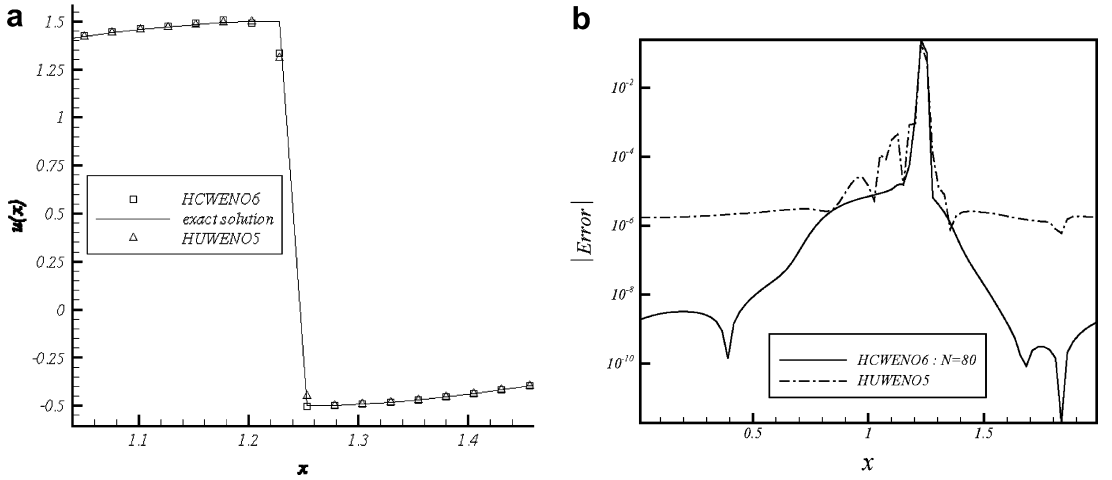

Fig. 9. Burgers equation. Case with shock. $N = 80$, $t = 3/2\pi$. Comparison between the HCWENO6 scheme and the HUWENO5 scheme. (a) Computed solution, (b) discretization error.

The mean flow is a right moving Mach 3 shock. If ε is small compared to the shock strength, the shock will go to the right of the computational domain, at approximately the non-perturbed shock speed and generate a sound wave that travels along with the flow behind the shock. At the same time, the small amplitude, low-frequency entropy waves are generated in front of the shock. After having interacted with the shock, these waves are compressed in frequency and amplified in amplitude.

The main goal of such a test is to check if the structure of the amplified waves is not lost after having crossed the shock wave. Since the entropy wave is very weak relative to the shock, any excessive numerical oscillation could alter the generated waves and the entropy waves.

In our computations, we take $\varepsilon = 0.01$. Accordingly, the amplitude of the amplified entropy waves predicted by a linear analysis, [20,21], is 0.08690716 (shown in the following figures as horizontal solid lines). The pre-shock wave number, k, is selected such that $k \in \{13, 26, 39\}$. To get rid of the transient waves due to the initialization, the numerical procedure is defined so that the shock crosses the computational domain twice. The numerical solution is examined when the shock reaches $x = 4.5$ for the second time. For those computations, the CFL is lowered to the value 0.30.

First, for $k = 13$, we use 400 grid points that is effectively 10 points in each wave length of the generated entropy wave. The results are shown in Fig. 13 (the mean flow has bee subtracted from the numerical solution). We can see that on this grid, the HCWENO6 scheme calculates the amplified entropy waves quite well, although their amplitude is slightly attenuated, Fig. 13(a). On a grid of 800 points, Fig. 13(b), the resolution becomes very good with the HCWENO6 scheme. To compare, we produce the numerical results obtained with 1200 grid points, by using the HUWENO5 scheme, Fig. 13(c); obviously, the scheme produces excessive damping of the entropy waves: the reason is given by the nonlinear weights that do not reach accurately their ideal values on such a grid. Lastly, Fig. 13(d) and (e) produces numerical results for $k = 26$, $N = 800$ and $k = 39$, $N = 1200$, respectively. Even if the amplitude of the entropy waves is slightly attenuated behind the shock, the HCWENO6 scheme keeps on giving good results.

Example 5 (*Propagation of sound waves through a transonic nozzle*, [22]). The computation of sound propagating through a choked nozzle presents a challenging problem for a shock-capturing scheme. To reduce the complexity of the problem, but retaining the basic physics and difficulties, this propagation problem is modelled by a one-dimensional acoustic wave transmission problem through a transonic nozzle, [22].

In this problem, an acoustic wave is introduced at the nozzle inflow region and the sound wave that travels downstream through the transonic nozzle and interacts with the shock is to be calculated. The amplitude of the incoming sound wave is $\varepsilon = 10^{-5}$, which is very small compared to the mean values of the flow. The nozzle flow is modelled by the one-dimensional Euler equations with variable nozzle area:

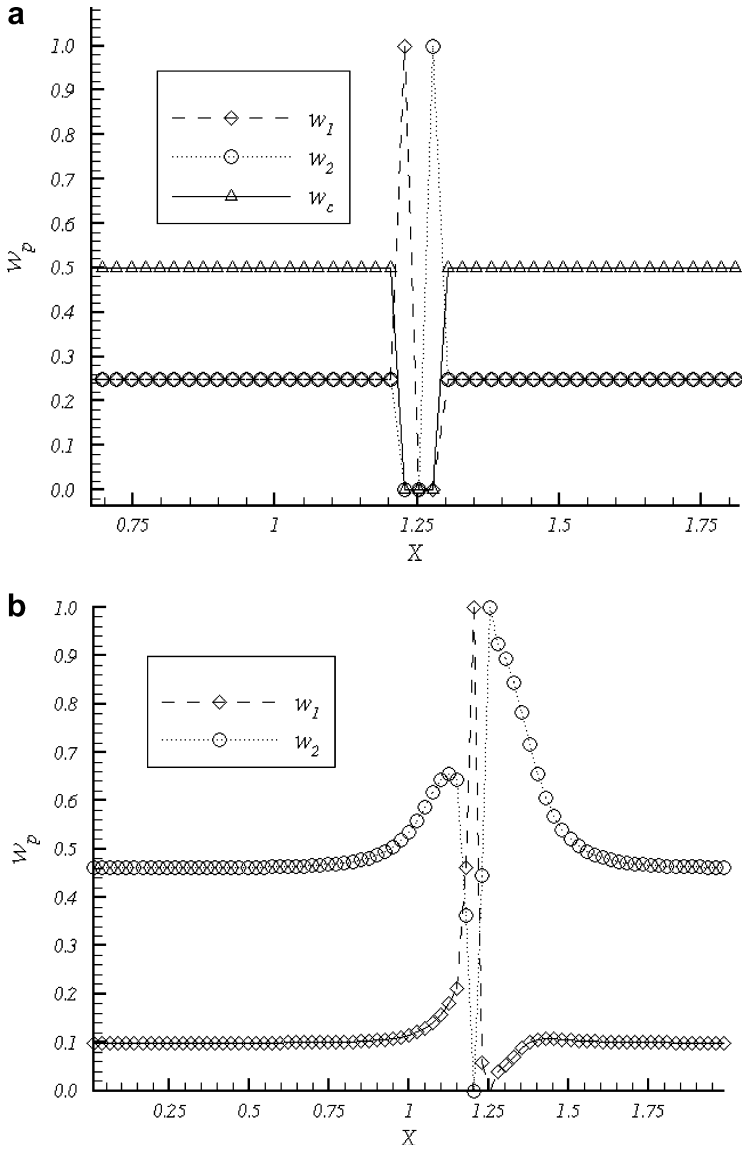

Fig. 10. Burgers equation. Case with shock. $N = 80$, $t = 3/2\pi$. Nonlinear weights: (a) HCWENO6 scheme, (b) HUWENO5 scheme.

Table 3
One-dimensional Euler equations $\rho(x, t = 0) = 1 + 0.2 \times \sin(\pi x)$, $u(x, t = 0) = 1$, $p(x, t = 0) = 1$; HCWENO6 scheme with periodic boundary conditions $t = 2$; $\Delta t = \Delta x^2/2$; L_1 and L_∞ errors of density ρ

N	L_1 error	L_1 order	L_∞ error	L_∞ order
10	7.15×10^{-4}	–	5.59×10^{-4}	–
20	8.92×10^{-6}	6.2	7×10^{-6}	6.3
40	1.21×10^{-7}	6.2	9.49×10^{-8}	6.2
80	1.75×10^{-9}	6.1	2.12×10^{-9}	6.1
160	3.14×10^{-11}	6	3.80×10^{-11}	6

Table 4
One-dimensional Euler equations $\rho(x,t=0)=1+0.2\times\sin(\pi x)$, $u(x,t=0)=1$, $p(x,t=0)=1$; HUWENO5 scheme with periodic boundary conditions $t=2$; $\Delta t=\Delta x^2/2$; L_1 and L_∞ errors of density ρ

N	L_1 error	L_1 order	L_∞ error	L_∞ order
10	5.44×10^{-3}	–	4.25×10^{-3}	–
20	1.33×10^{-4}	5	1.04×10^{-4}	5
40	3.64×10^{-6}	4.9	2.86×10^{-6}	4.9
80	1.06×10^{-7}	5.1	8.36×10^{-8}	5.1
160	3.22×10^{-9}	4.9	2.66×10^{-9}	4.8
320	1.0×10^{-10}	5	1.30×10^{-10}	4.9

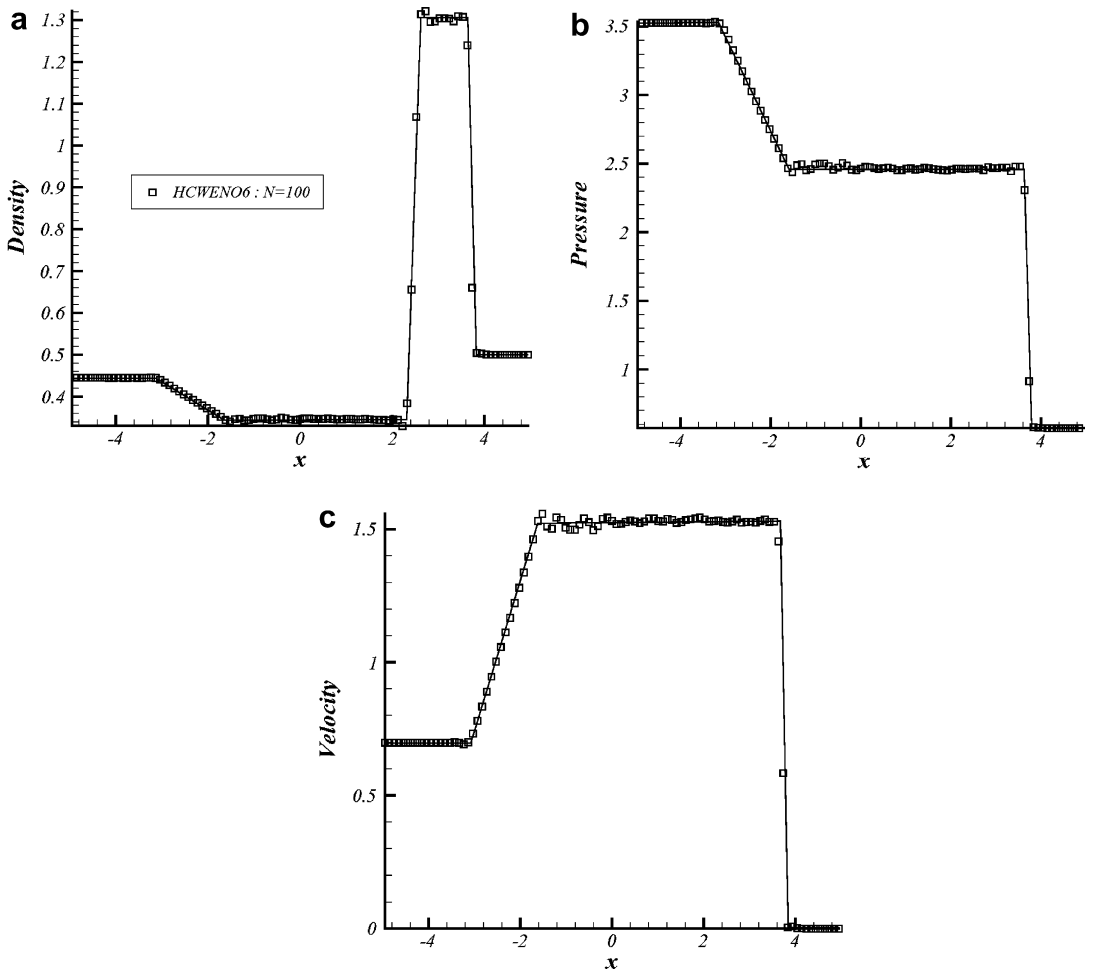

Fig. 11. The Lax problem. HCWENO6 scheme. ($N=100$, $t=1.30$, CFL $=0.5$). (a) Density, (b) pressure, (c) velocity.

$$\frac{\partial \mathbf{U}}{\partial t}+\frac{\partial \mathbf{F}(\mathbf{U})}{\partial x}=-\frac{1}{A}\frac{\mathrm{d}A}{\mathrm{d}x}\mathbf{U}' \qquad (46)$$
$$\mathbf{U}\equiv[\rho,\rho u,\rho E]^t,\quad \mathbf{F}\equiv[\rho u,\rho u^2+p,\rho uH]^t,\quad \mathbf{U}'\equiv[\rho u,\rho u^2,\rho uH]^t$$

The area of the nozzle is

$$A(x)=\begin{cases}0.536572-0.198086\times\exp\left(-\left(\mathrm{Log}(2)\left(\frac{x}{0.6}\right)^2\right)\right), & x>0\\ 1.0-0.661514\times\exp\left(-\left(\mathrm{Log}(2)\left(\frac{x}{0.6}\right)^2\right)\right), & x<0\end{cases}$$

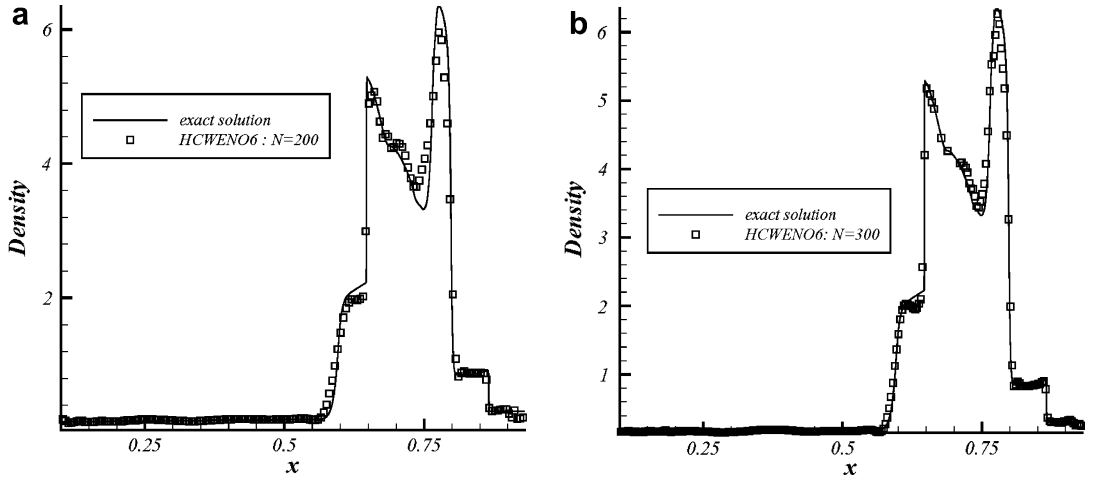

Fig. 12. Blast wave problem. Density ρ. $t = 0.038$, CFL = 0.5. HCWENO6 scheme: (a) $N = 200$, (b) $N = 300$.

Flow variables are non-dimensionalized by using the upstream values. The velocity scale is a_∞ (speed of sound), the length scale is D (diameter of the nozzle) and the density scale is the static density, ρ_∞.

Then, the mean flow at the inlet is

$$\begin{bmatrix} \bar{\rho} \\ \bar{u} \\ \bar{p} \end{bmatrix}_{\text{inlet}} = \begin{bmatrix} 1 \\ M_\infty \\ 1/\gamma \end{bmatrix} \tag{47}$$

The Mach number at the inlet, M_∞, is 0.2006533 and the pressure at the exit, p_{exit}, is 0.6071752, so that a shock is formed inside the nozzle. The shock location is then: $x_s = 0.3729$.

Just upstream of the shock wave, the Mach number is $M_1 = 1.465$ and downstream, $M_2 = 0.714$. The pressure ratio (intensity of the shock wave) is then $p_2/p_1 = 2.337$.

The incoming acoustic wave, with angular frequency, $\omega = 0.6\pi$, is described as

$$\begin{bmatrix} \rho \\ u \\ p \end{bmatrix}_{\text{acoustic}} = \varepsilon \begin{bmatrix} 1 \\ 1 \\ 1 \end{bmatrix} \sin\left[\omega\left(\frac{x}{1+M_\infty} - t\right)\right] \tag{48}$$

The acoustic perturbations for the derivatives are derived from (48).

In the present work, the acoustic wave will be computed directly by solving the nonlinear governing equations rather than solving the linearized equations (see [22] for some examples on the linearized problem). This makes it harder to compute the acoustic waves. The challenge is whether the small amplitude wave can still be captured in the computation by the HCWENO6 scheme. The computational domain is $-10 \leqslant x \leqslant 10$ and a non-uniform mesh, refined in the throat region, is used.

To begin, the steady state of the nozzle flow is computed. For the flow variables, the initial conditions are specified by using the mean exact solution of this problem.

The derivatives are then estimated by using a centred second-order finite-difference approximation. At the boundaries, the back pressure is specified at the outlet and the total pressure and density are specified at the inlet. The other needed information at both the inlet and outlet, are obtained using extrapolation from their neighbouring mesh points. Concerning the derivatives, all those quantities are set to zero at the inlet since the flow is assumed uniform. At the outlet, the pressure derivative is set to zero while the remaining quantities are extrapolated in order for the error to leave the computational domain without numerical reflections.

The steady-state solution of (46), obtained using a 120 points non-uniform mesh ($\Delta x_{\min} = 0.10$, $\Delta x_{\max} = 0.49$) with CFL = 0.80, is compared with the exact solution, Fig. 14(a). The solution is converged

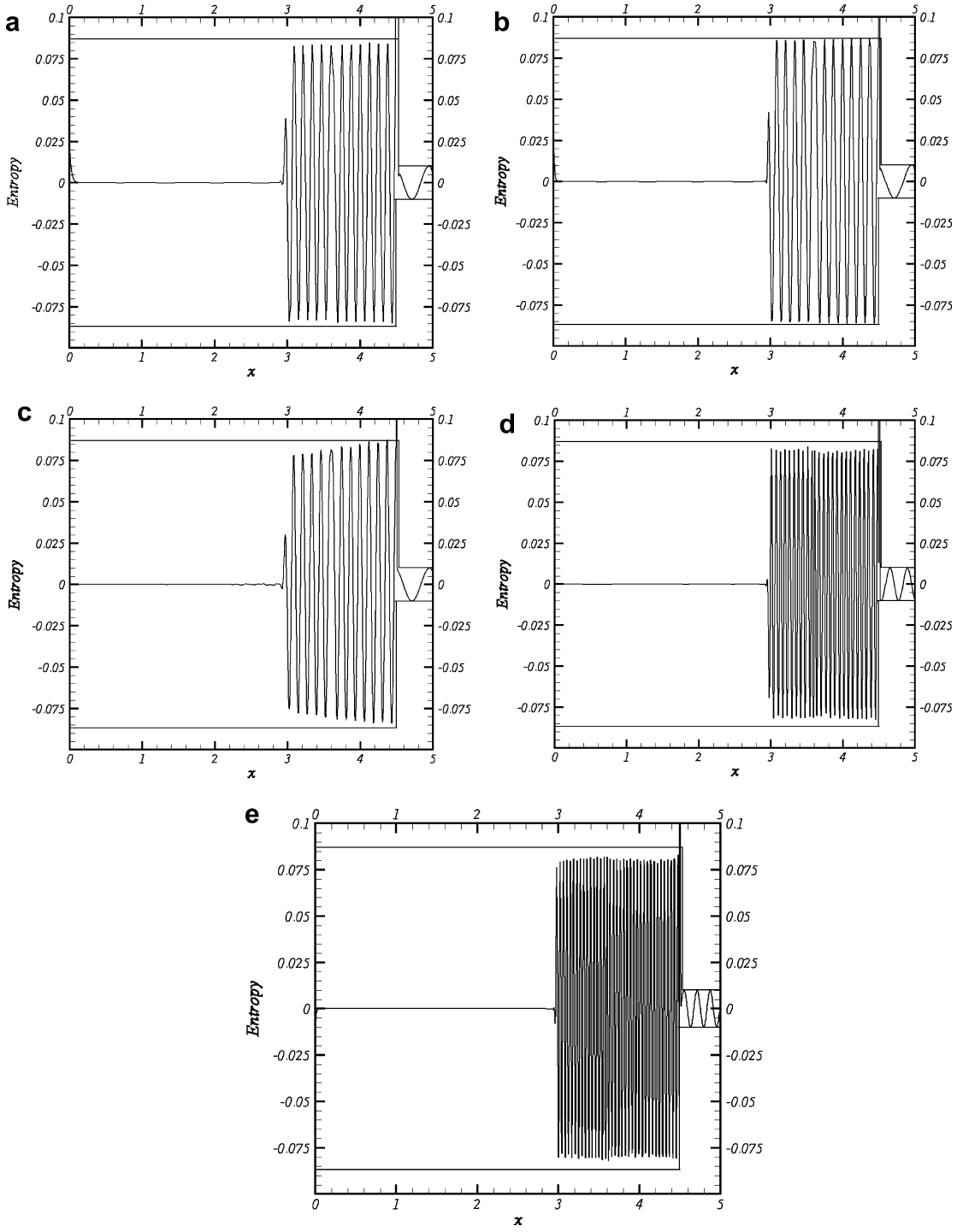

Fig. 13. Shock entropy wave interaction: $t = 3.38061$. (a) $k = 13$, $N = 400$; (b) $k = 13$, $N = 800$; (c) HUWENO5: $k = 13$, $N = 1200$; (d) $k = 26$, $N = 800$; (e) $k = 39$, $N = 1200$.

to machine precision, Fig. 14(b). It can be seen that flow properties are uniform in most region of the nozzle, but change dramatically near the nozzle throat, Fig. 14(a). Lastly, the shock is captured without any numerical oscillation. Note however, that the numerical parameters must be carefully selected to converge towards the

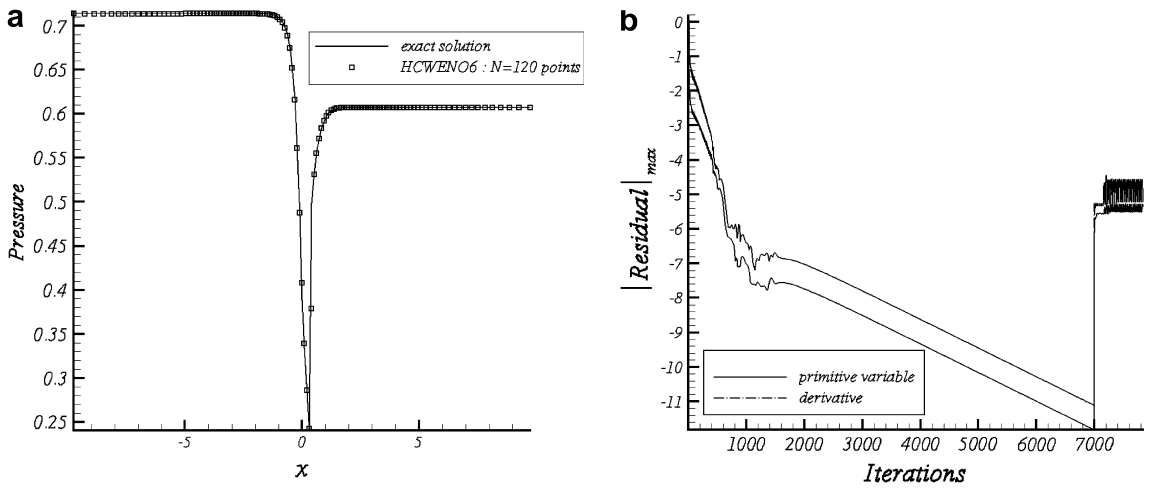

Fig. 14. Propagation of sound waves through a transonic nozzle. Steady-state solution. HCWENO6 scheme. CFL = 0.8, $N = 120$. (a) Mean pressure, (b) maximum residual.

steady-state: as indicated by the theoretical stability analysis, the stability domain of the HCWENO6 is altered by a strongly varying source term.

After the steady-state flow-field is computed, the acoustic wave propagation can be simulated using the same nonlinear solver. First, the initial conditions are specified using the steady-state solution previously calculated, then, at the inlet, the solution (48) is superimposed for the variables and its derivatives.

Numerical solutions of the acoustic pressure at $t = 14T$ are shown in Fig. 15 and compared with the analytical solution (given in [22]).

With only 100 grid points, the wave pattern is not correctly captured, Fig. 15(a), while a greatly improved result is produced using a 120 point non-uniform mesh, Fig. 15(b). However, the amplitude of the acoustic wave at the shock location is lower than that indicated by the analytical solution: this is due to the first-order error introduced by the scheme right at this place. In spite of this difficulty, one can note that the profiles of the acoustic pressure both upstream and downstream the shock location, agree very well with the analytical solution, Fig. 15(b).

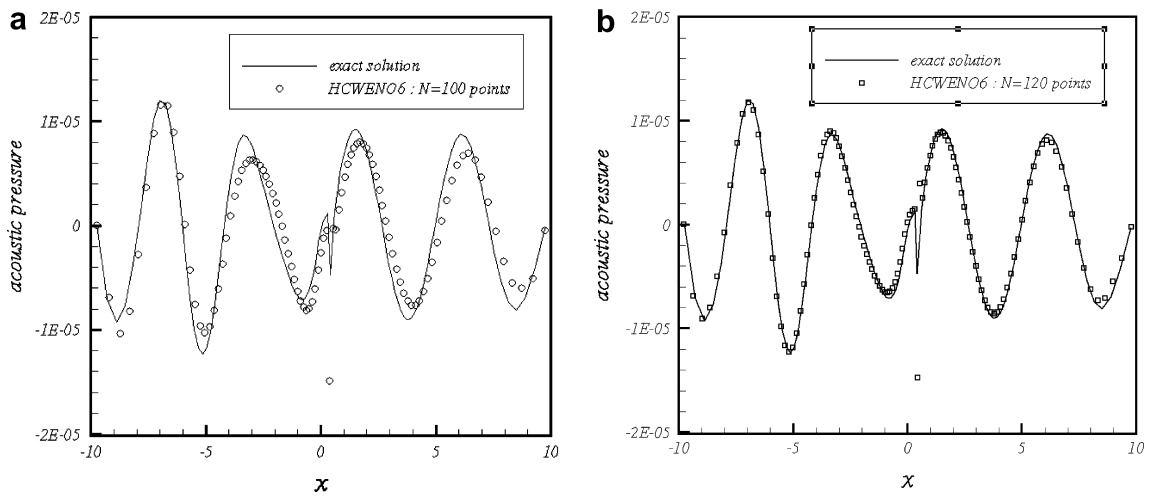

Fig. 15. Propagation of sound waves through a transonic nozzle. Acoustic pressure at $t = 14T$. HCWENO6 scheme. CFL = 0.8. (a) $N = 100$, $\Delta x_{\min}/\Delta x_{\max} = 0.24$. (b) $N = 120$, $\Delta x_{\min}/\Delta x_{\max} = 0.20$.

As already mentioned, any high-order scheme captures the shock with a first-order accuracy; however, those results demonstrate that this defect does not alter the smooth part of the solution: the multi-scale structure of the solution is preserved after having crossed the shock wave. In other words, this result means that the numerical error generated by capturing the shock remains confined and does not propagate. Thus, this property explains the good results obtained with the HCWENO6 scheme. The main advantage of such a scheme comes from its compactness and the definition of its nonlinear weights: this enables to generate a local first-order correction.

5. Concluding remarks

In this paper, we constructed a new WENO Hermite interpolation for 1D hyperbolic conservation laws. This interpolation results from a convex centred combination of Hermite polynomials. Combined with a third-order TVD Runge–Kutta procedure for the time-integration, we demonstrated that this procedure generates a sixth-order scheme in smooth regions and for small CFLs. Furthermore, a new formulation of the nonlinear weights in the convex combination, enables to generate a nonlinearly stable reconstruction near discontinuities. For this purpose, the scheme becomes of the fourth-order in the cells close to the shock and can even become first-order at the location of the shock if the Hermite interpolation generates oscillations.

Then, it becomes possible to compute, with a high degree of accuracy, multi-scales problems containing discontinuities. Lastly, the choice of a central WENO procedure enables to widen the domain of application of the scheme to non-uniform meshes.

However, some work is needed to improve this method before a multi-dimensional extension. This is especially true in some special cases such as, for example, problems with source terms. Indeed, although we successfully computed some of those problems, the computations necessitated a careful tuning of the parameters of the scheme (CFL, grid stretching). An asymptotic stability analysis even demonstrated that the scheme could become unstable if the number of grid points becomes insufficient.

It is important to deal with this difficulty. For example, in nonlinear aero-acoustics, source terms must be incorporated into the equations if one wants to model nonlinear regions of source of sound. This point will be emphasized in a next future.

Similarly, the generation of a specific Riemann solver for a Hermite formulation of a hyperbolic problem will be addressed. In such a case, the benefit hoped will be an increased domain of stability for the discretization and an improved description of the physics. Moreover, to maintain the high performances of the HCWENO reconstruction for complex geometries, the present procedure will be extended to multi-dimensional problems.

Acknowledgment

The author wishes to thank Dr. G.B. Deng (Ecole Centrale de Nantes – France) with recognition who provided a technical support essential to this work.

References

[1] A. Harten, B. Engquist, S. Osher, S. Chakravarthy, Uniformly high-order essentially non-oscillatory schemes, III, J. Comput. Phys. 71 (1987) 231–303.
[2] C.-W. Shu, Essentially non-oscillatory and weighted essentially non-oscillatory schemes for hyperbolic conservation laws, ICASE Report 97-65.
[3] S.K. Lele, Compact finite-difference schemes with spectra-like resolution, J. Comput. Phys. 103 (1992) 16.
[4] B. Van-Leer, Towards the ultimate conservative difference scheme: III. A new approach to numerical convection, J. Comput. Phys. 23 (1977) 276–299.
[5] S. Pirozzoli, Conservative hybrid compact WENO schemes for shock–turbulence interaction, J. Comput. Phys. 178 (2002) 81–117.
[6] Yu-X. Ren, M. Liu, H. Zhang, A characteristic-wise hybrid compact WENO scheme for solving hyperbolic conservation laws, J. Comput. Phys. 192 (2003) 365–386.
[7] F. Bouchut, C. Bourdarias, B. Perthame, A MUSCL method satisfying all the numerical entropy inequalities, Math. Comput. 65 (1996) 1439–1461.

[8] R.L. Dougherty, A.S. Edelman, J.M. Hyman, Nonnegativity-, monoticity-, or convexity preserving cubic quintic Hermite interpolation, Math. Comput. 52 (1989) 471–494.
[9] T. Nakamura, R. Tanaka, T. Yabe, K. Takizawa, Exactly conservative semi-Lagrangian scheme for multi-dimensional hyperbolic equations with directional splitting technique, J. Comput. Phys. 174 (2001) 171–207.
[10] J. Qiu, C.-W. Shu, Hermite WENO schemes and their applications as limiters for Runge–Kutta discontinuous Galerkin method: one-dimensional case, J. Comput. Phys. 193 (2004) 115–135.
[11] J. Qiu, C.-W. Shu, Hermite WENO schemes and their applications as limiters for Runge–Kutta discontinuous Galerkin method: two-dimensional case, Comput. Fluids 34 (2005) 642–663.
[12] D. Levy, G. Pupo, G. Russo, Compact central WENO schemes for multidimensional conservation laws, SIAM J. Sci. Comput. 22 (2000) 656–672.
[13] C.-W. Shu, S. Osher, Efficient implementation of essentially non-oscillatory shock-capturing schemes, J. Comput. Phys. 77 (1988) 439–471.
[14] R.G. Hindman, On shock-capturing methods and why they work, AIAA-paper-88-0622.
[15] R.J. Leveque, Numerical Methods for Conservation Laws, Birkhaüser Verlag, 1990, 115-121.
[16] A.K. Henrick, T.D. Aslam, J.M. Powers, Mapped weighted essentially non-oscillatory schemes: achieving optimal order near critical points, J. Comput. Phys. 207 (2005) 542–567.
[17] A. Harten, P.D. Lax, B. Van-Leer, On upstream differencing and Godunov-type schemes for hyperbolic conservation laws, SIAM Rev. 25 (1983) 35.
[18] C. Hirsch, Numerical Computation of Internal and External Flows, vol. I, Ed. Wiley & Sons, 1987, pp. 371–401.
[19] J. Casper, M.H. Carpenter, Computational considerations for the simulation of shock-induced sound, NASA-TM 110222, 1995.
[20] J. Mc Kenzie, K. Westphal, Interaction of linear waves with oblique shock waves, Phys. Fluids 11 (1968) 2350–2362.
[21] T.A. Zang, M.Y. Hussaini, D.M. Bushnell, Numerical computations of turbulence amplification in shock wave interactions, AIAA J. 22 (1984) 13–21.
[22] Third computational aeroacoustics workshop on benchmark problems, NASA/CP-2000-209790.
[23] J. Qiu, C.-W. Shu, On the construction, comparison, and local characteristic decomposition for high-order central WENO schemes, J. Comput. Phys. 183 (2002) 187–209.
[24] P. Woodward, P. Colella, The numerical simulation of two-dimensional fluid flow with strong shocks, J. Comput. Phys. 54 (1984) 115–173.